CrossMark

Large-scale numerical simulations of polydisperse particle flow in a silo

S. M. Rubio-Largo[1] · **D. Maza**[1] · **R. C. Hidalgo**[1]

Abstract Very recently, we have examined experimentally and numerically the micro-mechanical details of monodisperse particle flows through an orifice placed at the bottom of a silo (Rubio-Largo et al. in Phys Rev Lett 114:238002, 2015). Our findings disentangled the paradoxical ideas associated to the *free-fall arch* concept, which has historically served to justify the dependence of the flow rate on the outlet size. In this work, we generalize those findings examining large-scale polydisperse particle flows in silos. In the range of studied apertures, both velocity and density profiles at the aperture are self-similar, and the obtained scaling functions confirm that the relevant scale of the problem is the size of the aperture. Moreover, we find that the contact stress monotonically decreases when the particles approach the exit and vanish at the outlet. The behavior of this magnitude is practically independent of the size of the orifice. However, the total and partial kinetic stress profiles suggest that the outlet size controls the propagation of the velocity fluctuations inside the silo. Examining this magnitude, we conclusively argue that indeed there is a well-defined transition region where the particle flow changes its nature. The general trend of the partial *kinetic pressure* profiles and the location of the transition region results the same for all particle types. We find that the partial kinetic stress is larger for bigger particles. However, the small particles carry a higher fraction of kinetic stress respect to their concentration, which suggest that the small particles have larger velocity fluctuations than the large ones and showing lower strength of correlation with the global flow. Our outcomes explain why the *free-fall arch* picture has served to describe the polydisperse flow rate in the discharge of silos.

1 Introduction

Predicting the mass flow rate during the discharge of silos has been thoroughly attempted in the past years [2–5]. In general, theoretical frameworks assume that close to the orifice there is a region where the inter-particle forces diminish. Hence, below this vault, the particles move as a dilute gas falling only due to gravity. This was postulated by Brown and Richards [3], who introduced the concept of *free-fall arch*. Nowadays, this concept is widely used and researchers relate it to the Beverloo' correlation [6] and more recent approaches [7,8]. However, the idea of a *free-fall arch* implies the existence of a stress discontinuity, which is difficult to justify theoretically [9,10]. In addition, recent experimental efforts aimed at proving the existence of such a transition have provided non-conclusive outcomes [11,12].

On the other hand, there are several experimental restrictions in examining granular flows. A complete access to the 3D behavior of the grains is not feasible. Hence, there is a real need to perform numerical simulations in this framework. Discrete element modeling (DEM) is widely accepted as an effective method to address engineering problems concerning dense granular media [13]. Moreover, in typical applications, the formulation of granular macroscopic fields is also necessary. Thus, the micro-mechanical details, *i.e.,* velocity and position of individual particles, allow one to find the continuum field profiles using a coarse-grained average technique [14–17]. Furthermore, with this homogenization approach, the static and dynamic parts of the stress tensor

✉ R. C. Hidalgo
raulcruz@unav.es

[1] Department of Physics and Applied Mathematics,
University of Navarra, Pamplona, Spain

Springer

are deduced in terms of contact forces and velocity fluctuation, respectively. The ultimate aim is to achieve a continuum mechanical description of granular flows based on the micro-mechanics, which will help us to understand how particle shape and polydispersity affect the pressure distribution and jamming in granular flows [4,18–30].

In a previous work, we examined experimentally and numerically the micro-mechanical details of monodisperse particle flows through an orifice placed at the bottom of a silo [1]. Our findings disentangle the paradoxical ideas associated with the *free-fall arch* concept, which has historically served to justify the dependence of the flow rate on the outlet size. In this work, we generalize those findings, examining polydisperse 3D particle flows in silos. It is very well known, however, that the response of polydisperse systems to external excitation is difficult to predict because the local interactions often lead to undesired segregation of particles [31–33]. For sake of simplicity and to minimize segregation effects, we have used a narrow particles size distribution, which enforced a mass flow pattern in a silo rather than a funnel flow pattern [34,35]. The paper is organized as follows: in Sect. 2, we introduce the numerical method and the theoretical framework of the coarse-grained formulation [14]. Then, in Sect. 3 we explain the implementation of the coarse-grained methodology, which has been used to process the numerical data, allowing to clarify the nature of the granular flow close to the orifice.

2 Model description

We introduce a hybrid CPU–GPU discrete element algorithm for a polydisperse system of spheres. This numerical algorithm is an improved version of the monodisperse case [1]. As a first step, to mimic the real experimental scenario, we generate a granular gas of $N = 393, 216$ monodisperse spheres of radius $r_b = 1/64$ m. The particles are located at random positions within a cylindrical container with a flat bottom and radius R_c. Then, they settle under the effect of gravity and the packing relaxes until its kinetic energy is several orders of magnitude smaller than its potential energy. As a second step, granular polydispersity is introduced by randomly reducing the particle size. We use seven types of particle, with the largest radius being r_b, the smallest radius being $r_s = \frac{r_b}{2} + \Delta$ following an arithmetic progression with difference $\Delta = \frac{r_b}{16}$. Thus, after implementing this procedure, the system is composed of seven different sizes distributed uniformly (see sketch of Fig. 1). As a final step, the particles are allowed to leave the system through a circular outlet of radius R that is located at the bottom. A snapshot of the three-dimensional silo is shown in Fig. 1.

In the simulation, each particle i has three translational degrees of freedom and a quaternion formalism has been
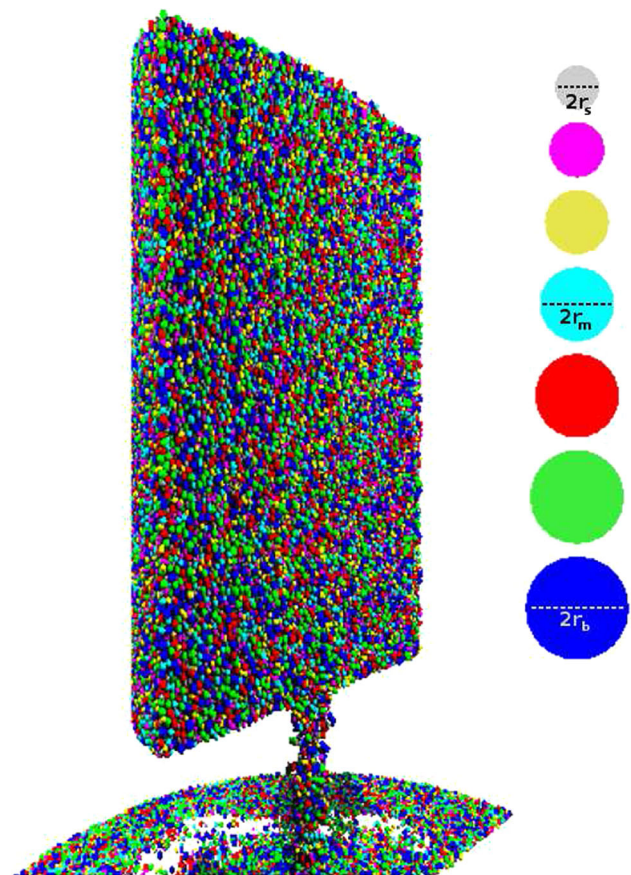
Fig. 1 Snapshot of a numerical three-dimensional silo where the *color of the particles* indicates their size. The *sketch of particle* types illustrates the system polydispersity

implemented for describing the 3D angular rotations [36,37]. The interaction between particle i and particle j is decomposed in normal and tangential directions. In our approach, the normal interaction is defined by a linear contact, and to introduce dissipation, a velocity-dependent viscous damping is assumed. The tangential force also contains an elastic term and a tangential frictional term accounting for static friction between the grains. More details about the numerical implementation can be found in the Appendix 1.

2.1 Coarse-graining formulation

In order to explore the dynamical and mechanical properties of the particle flow, a coarse-graining methodology is used to analyze the results [14–17]. First, we access to the position and velocities of every particle. According to [14–17], the macroscopic mass density of a granular flow, $\rho(\mathbf{r})$, at time t is defined by

$$\rho(\mathbf{r}, t) = \sum_{i=1}^{N} m_i \phi(\mathbf{r} - \mathbf{r}_i(t)), \qquad (1)$$

where the sum runs over all the particles within the system and the coarse-grained (CG) function, $\phi(\mathcal{R})$. In our case, we use a truncated Gaussian coarse-graining function $\phi(\mathcal{R}) = A_w e^{-(|\mathcal{R}|/2w)^2}$ with cutoff $r_c = 4w$ where the value of w defines the coarse-grained scale. A_w is calculated in order to guarantee the normalization condition. Thus, the flow solid fraction can be found $\varphi(\mathbf{r}, t) = \rho(\mathbf{r}, t)/\rho_p$, where ρ_p is the material density (see Appendix 1).

Similarly, the macroscopic mass density of the component j, $\rho_j(\mathbf{r})$, at time t is defined by

$$\rho_j(\mathbf{r}, t) = m_j \sum_{i=1}^{N_j} \phi(\mathbf{r} - \mathbf{r}_i(t)), \tag{2}$$

where the sum runs over the N_j particles of radius r_j. Thus, the partial solid fraction can be found as $\varphi_j(\mathbf{r}, t) = \rho_j(\mathbf{r}, t)/\rho_p$.

In the same way, the coarse-grained momentum density function $P(\mathbf{r}, t)$ is defined by

$$P(\mathbf{r}, t) = \sum_{i=1}^{N} m_i \mathbf{v}_i \phi(\mathbf{r} - \mathbf{r}_i(t)), \tag{3}$$

where the $\mathbf{v}_i$ represents the velocity of particle i. The macroscopic velocity field $\mathbf{V}(\mathbf{r}, t)$ is then defined as the ratio of momentum and density fields,

$$V(\mathbf{r}, t) = P(\mathbf{r}, t)/\rho(\mathbf{r}, t). \tag{4}$$

In order to define the mean stress field, we use a very elegant and mathematically consistent definition of mean stress $\bar{\sigma}_{\alpha\beta}$ introduced by Goldhirsch [14]. Following this approach, the total stress field $\sigma_{\alpha\beta}$ is composed by a kinetic stress field $\sigma^k{}_{\alpha\beta}$ and a contact stress field $\sigma^c{}_{\alpha\beta}$. They are defined as follows: the mean contact stress tensor reads as

$$\sigma^c_{\alpha\beta}(\mathbf{r}) = -\frac{1}{2} \sum_{i=1}^{N} \sum_{j=1}^{Nc_i} f_{ij\alpha} r_{ij\beta} \int_0^1 \phi(\mathbf{r} - \mathbf{r}_i + s\mathbf{r}_{ij}) ds, \tag{5}$$

where the sum runs over all the contacting particles i, j, whose center of mass are at $\mathbf{r}_i$ and $\mathbf{r}_j$, respectively. Moreover, $\mathbf{f}_{ij}$ accounts for the force exerted by particle j on particle i and $\mathbf{r}_{ij} \equiv \mathbf{r}_i - \mathbf{r}_j$.

On the other hand, the kinetic stress field reads as,

$$\sigma^k_{\alpha\beta}(\mathbf{r}) = -\sum_i^{N} m_i v'_{i\alpha} v'_{i\beta} \phi(\mathbf{r} - \mathbf{r}_i(t)), \tag{6}$$

where the sum runs over all the particles, $\mathbf{v}'_i$ is the velocity fluctuation of particle i, respect to the mean field.

$$\mathbf{v}'_i(\mathbf{r}, t) = \mathbf{v}_i(t) - \mathbf{V}(\mathbf{r}, t). \tag{7}$$

Examining a polydisperse particle flow, we can focus our attention on the way the kinetic stress is distributed between particles of different sizes [38]. We define, the partial kinetic stress field $s^j_{\alpha\beta}$ related with particle type j, which reads as,

$$s^j_{\alpha\beta}(\mathbf{r}) = -m_j \sum_p^{N_j} v'_{p\alpha} v'_{p\beta} \phi(\mathbf{r} - \mathbf{r}_p(t)), \tag{8}$$

where the sum runs over the N_j particles of type j, and $\mathbf{v}'_p$ is the fluctuation of the velocity of particle p, respect to the mean field. Note that $\sigma^k_{\alpha\beta} = \sum_{types} s^j_{\alpha\beta}$.
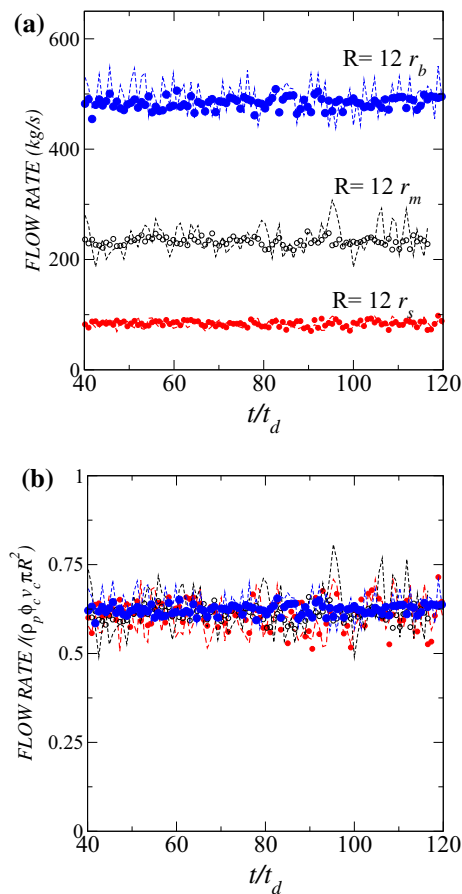
Based on the previous theoretical framework, we have implemented a post-processing tool, which has allowed us to examine the $3D$ kinetic fields. Complementary, all the micro-mechanical properties of the simulated flow have been explored in detail.

3 Results and discussion

Here, we examine the micro-mechanical properties of a polydisperse granular system during a silo discharge. The complexity of the particle flow has been described accessing to all the micro-mechanical details. We explore the behavior of the grains both in the proximities of the orifice and the upper part of the silo.

First, we focus our attention on the particle flow rate through the orifice placed at the bottom of the silo. Numerical outcomes obtained for several apertures are presented in Fig. 2a. The time evolution of the mass flow rate $W_f(t)$ is shown in terms of the characteristic time $t_d = \sqrt{\frac{2r_b}{g}}$, which is the time elapse in which a free falling particle moves a distance proportional to its own diameter. Note that $W_f(t)$ is the total mass that flow through the outlet, which can be accurately measured. For comparison, we also estimate the mass reduction of the silo $W_r(t)$ by measuring the velocity of the upper surface v_s (velocity of the highest particle). Thus, W_r is estimated as $W_r(t) = v_s \pi R_c^2 \rho_p \varphi_{\text{bulk}}$, where R_c is the radius of the container and φ_{bulk} stands for the bulk solid fraction, which is determined at a slab touching the top surface of the material. In our numerical experiment, we have found $\varphi_{\text{bulk}} = 0.60 \pm 0.02$. The excellent agreement between the values of $W_r(t)$ and $W_f(t)$ indicates that the segregation effects are very weak.
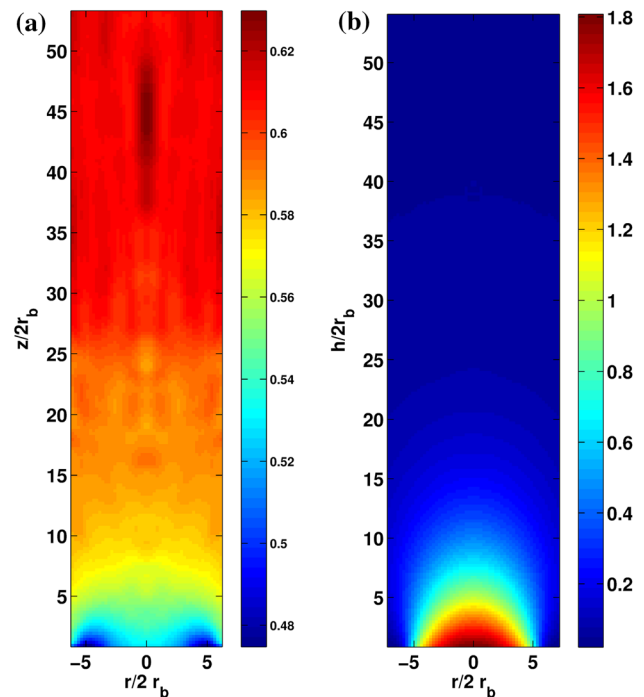
Additionally, in Fig. 2b, the values of flow rate are presented, but rescaled by $\rho_p \varphi_c(R) v_c(R) \pi R^2$, where $\varphi_c(R)$ and $v_c(R)$ are the volume fraction and velocity at the orifice, respectively. The collapse of the curves demonstrates that regardless the system polydispersity, the only relevant length scale governing the silo flow is the aperture size R. These results resemble very recent experimental findings obtained
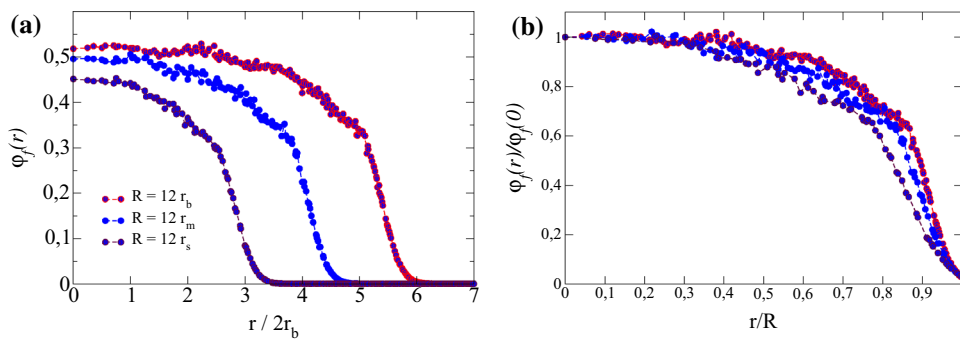
Fig. 3 Solid fraction **a** and vertical velocity **b** fields obtained for the 3D numerical polydisperse particle flow in a silo. In all cases $R = 12r_b$ and a Gaussian coarse-graining function $\phi(\mathcal{R})$ with $w = 2r_b$ was used. In the figures, the vertical coordinate, z, indicates the height from the *bottom* of the silo, and the horizontal coordinate, r, the distance to center of the silo

Fig. 2 In **a** the time evolution of the flow rate in terms of the characteristic time $t_d = \sqrt{\frac{2r_b}{g}}$ is shown for different outlet sizes. Outcomes obtained for several apertures are presented. The *symbols* and *lines* correspond to $W_f(t)$ and $W_r(t)$, respectively. In **b** the values of flow rate are rescaled $\rho_p \varphi_c(R) v_c(R) \pi R^2$

for 3D bidisperse systems [39]. Moreover, it is noticeable from the results that the system quickly evolves to a steady state characterized by a constant flow rate. This fact allows us to use the coarse-graining methodology described in Sect. 2.1 to examine the micro-mechanical details of the particle flow [14–17]. Thus, the results presented next correspond to time-averaged values at the steady state.

In Fig. 3a, we illustrate as a color map the spatial dependence of the solid fraction $\varphi(\mathbf{r})$ for a silo with an orifice of $R = 12r_b$. The fields are deduced using a Gaussian coarse-graining function $\phi(\mathcal{R})$ with $w = 2r_b$. The level of rendering and the coarse-graining scale lead to an accurate description of the solid fraction field. The excluded volume effect of the orifice border is seen. The velocity field in the vertical direction v_z is presented in Fig. 3b. Note that both coarse-grained magnitudes display monotonic behavior with the height. When approaching the orifice, the velocity v_z increases, while the solid fraction $\varphi_f(\mathbf{r})$ decreases.

For comparison with the behavior of monodisperse systems [1], we check the radial dependency of the solid fraction $\varphi_f(\mathbf{r})$ and $v_z(\mathbf{r})$ at the orifice. We systematically study the system response, changing the orifice size R and the outcomes are shown in Figs. 4 and 5. It is noticeable that both fields reach maximum values ($\varphi_f(0)$ and $v_z(0)$) at the center of the outlet, while diminish close to the border. Interestingly, the data values collapse when plotting $\varphi_f(r)/\varphi_f(0)$ versus r/R and $v_z(r)/v_z(0)$ versus r/R. Thus, we can argue that R is the relevant length scale when examining $v_z(r)$ and $\varphi_f(r)$ at the orifice. Furthermore, the characteristic velocity at the orifice scales is $v_z(R) \sim \sqrt{R}$. These results resemble similar findings obtained in experiments of two-dimensional monodisperse systems [8] and three-dimensional bidisperse systems [39].

Additional micro-mechanical details of the particle flow can be obtained examining the stress fields. In Fig. 6, we plot the spatial behavior of the *contact pressure*, which is defined as the trace of the contact stress field. Note that the *contact pressure* is a monotonic decreasing function of the height. Furthermore, its behavior correlates to the increase of the dilatancy, which achieves a maximum value at the outlet. Here, it is important to remark that the values of contact pressure were nearly independent of the outlet size. Accordingly,

Fig. 4 In **a** solid fraction profiles at the orifice $\varphi_f(r)$ (averaged in the azimuthal direction) obtained for a different outlet radius. **b** The same data collapsed by the size of the orifice

Fig. 5 In **a** velocity profiles at the orifice $v_z(r)$ (averaged in the azimuthal direction) obtained for a different outlet radius. **b** The same data collapsed by the size of the orifice. The continuous line corresponds to $\sqrt{1-(r/R)^2}$
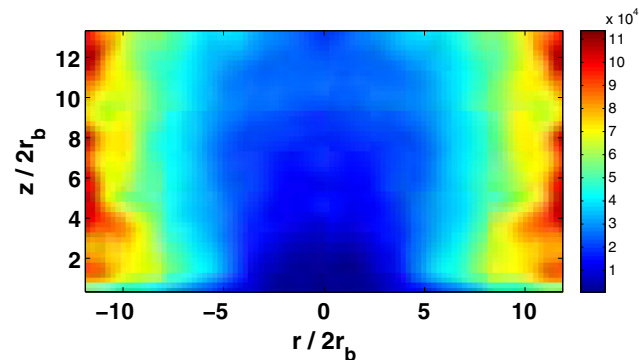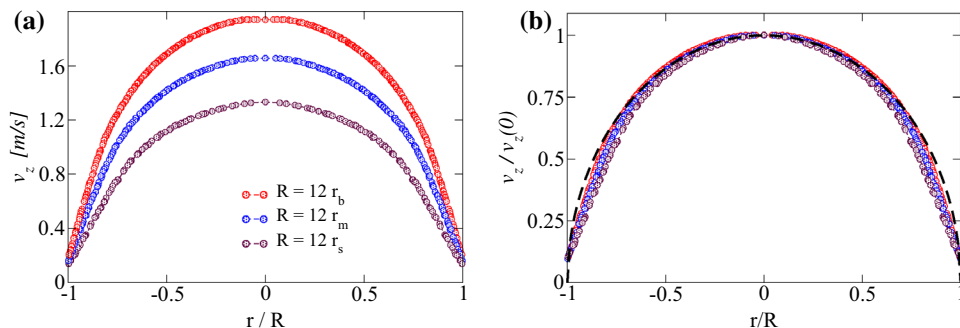
Fig. 6 *Contact pressure* field obtained for the 3D numerical polydisperse particle flow in a silo with an aperture size $R = 12r_b$ (data averaged in the azimuthal direction). The post-processing is done using a Gaussian coarse-graining function $\phi(\mathcal{R})$ with $w = r_b/2$. In the figures, the vertical coordinate, z, indicates the height from the bottom of the silo, and the horizontal coordinate, r, the distance to center of the silo

a region resembling a *free-fall arch* cannot be inferred from these findings.

Additionally, we analyze the strength of the total *kinetic pressure* field, calculating the trace of the kinetic stress tensor $\sigma_{\alpha\beta}^k(\mathbf{r})$ as defined by Eq. (6). In Fig. 7, we illustrate the *kinetic pressure* fields obtained for different sizes of the orifice. Although the strength of the *kinetic pressure* is several orders of magnitude smaller than the *contact pressure*, its spatial pattern reveals novel micro-mechanical details. Thus, $\sigma_{\alpha\beta}^k(\mathbf{r})$ conclusively establishes the existence of a well-defined transition region. In all cases, our numerical outcomes show that

far from the orifice, the particles follow the global macroscopic flow. This fact is related to the diminishing of the *kinetic pressure* with the height and indicates that the mass transport within the silo is mainly advective. However, as the particles get closer to the exit, their individual movement decorrelates to the global flow. Accordingly, $\sigma_{\alpha\beta}^k(\mathbf{r})$ shows a maximum value at the transition surface. After crossing, the particles fall by gravity and the total stress gradient slowly diminishes as one gets closer to the outlet.

For sake of simplicity, we focus on the evolution of the *kinetic pressure* along the vertical direction z at the center of the orifice. Astonishing, the kinetic pressure profiles can be collapsed, when normalizing the vertical coordinate with R. As we pointed out earlier, far from the outlet, particles follow a global macroscopic laminar flow where advection dominates their movements and, as consequence, the kinetic pressure is negligible. As the height decreases, the kinetic pressure grows exponentially (see inset of Fig. 8) until it reaches a well-defined maximum the location of which, $h_c(R)$, depends on the aperture size R. The quality of the collapse is lower on the upper part of the silo due to system size effects.
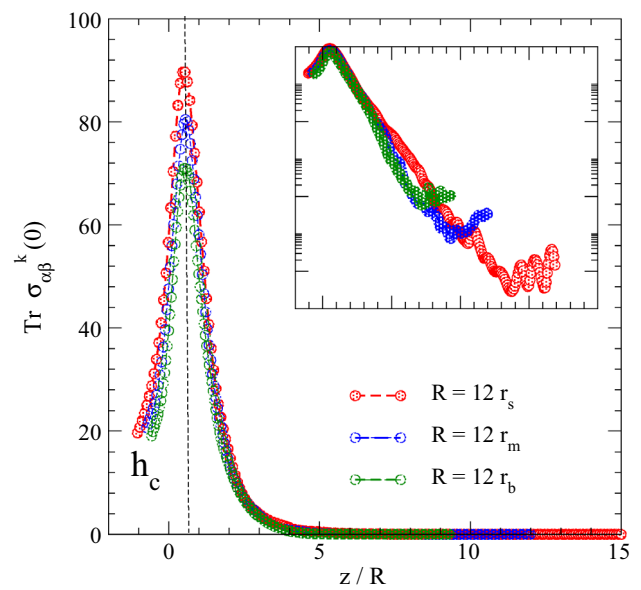
In Fig. 9 we study the robustness of our procedure to changes in the coarse-graining scale. To this end, the postprocessing of the data is performed using different values of w. As it noticeable, though the values of $\sigma_{\alpha\beta}^k$ depends on w [16,17,40], the findings are totally compatible and the location of transition region $h_c(R)$ remains invariant. Thus, we can conclude that though the kinetic stress is much smaller than the contact stress, the scaling of its spatial profile with R

(a)

(b)

(c)
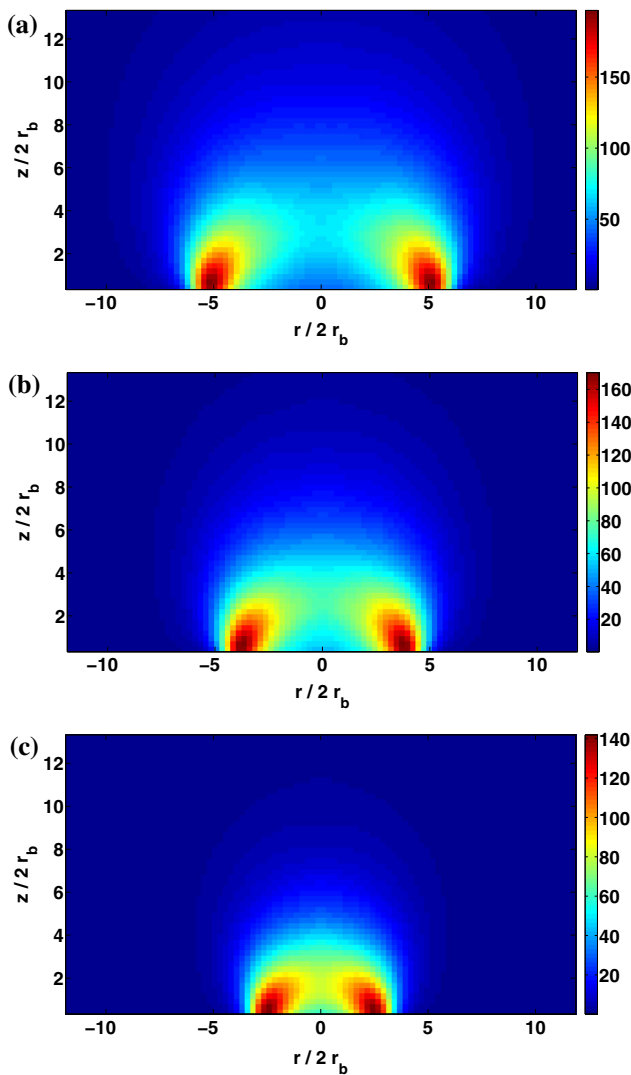
Fig. 7 Color maps of the 3D *kinetic pressure* profiles (data averaged in the azimuthal direction). In all cases, the post-processing is done using a Gaussian coarse-graining function $\phi(\mathcal{R})$ and $w = r_p$. Outcomes for different aperture sizes are shown [**a** $R = 12r_b$, **b** $R = 12r_m$ and **c** $R = 12r_s$]

Fig. 8 Vertical profiles of the *kinetic pressure* at the center of the silo $r = 0$ as a function of z/R. In **a** outcomes for different outlet sizes R are shown, the data collapse when normalizing the vertical coordinate z with the size of the outlet R. The *inset* shows the same in semi-log scale
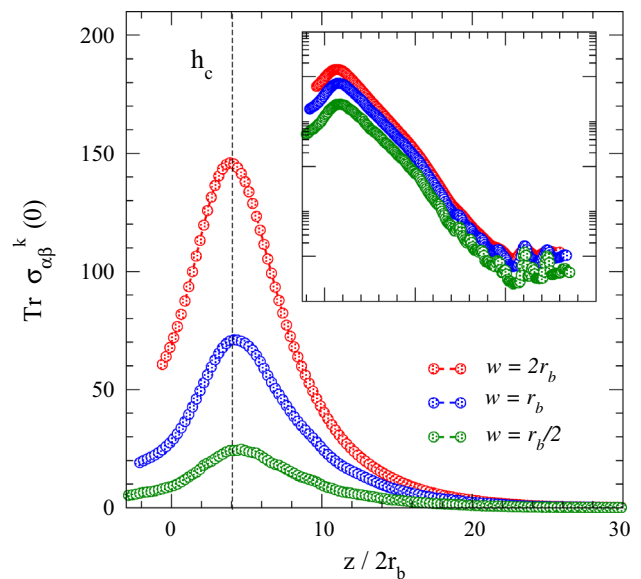
Fig. 9 Vertical profiles of the *kinetic pressure* at the center of the silo $r = 0$ and as a function of $z/2r_b$. The fields are deduced using a Gaussian coarse-graining function $\phi(\mathcal{R})$ with different values of w. The *inset* shows the same in semi-log scale

suggests its relevance explaining the discharge process. Similar findings were obtained experimentally and numerically in monodisperse systems [1].

We gain a better understanding of the role that the size of the particle plays on the flow process, examining the cumulative *kinetic pressure*. The cumulative values are obtained using Eq. (6), but calculating the sum constrained to the particle size, *i.e.,* including particles with $(r > r')$. The values of the cumulative *kinetic pressure* along the vertical direction z at the center of the orifice are shown in Fig. 10. Note that this magnitude equals the total kinetic stress in the limit case $(r > r_s)$. It is noticeable from the results that the kinetic stress is not shared uniformly among the different particle types. However, the general trend of the *kinetic pressure* profiles

close and far from the orifice is very similar (see inset of Fig. 10). Moreover, we found that in all cases, the location of the transition region $h_c(R)$ remains invariant.

We also examine systematically the behavior of the partial kinetic stress $s^j_{\alpha\beta}(\mathbf{r})$ [defined by Eq. (8)], which accounts for the kinetic stress stored in each type of particle. Intuitively, one could relate the difference in kinetic stress with
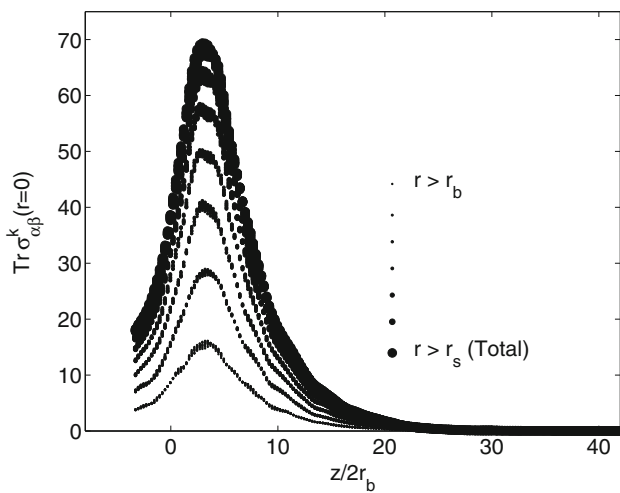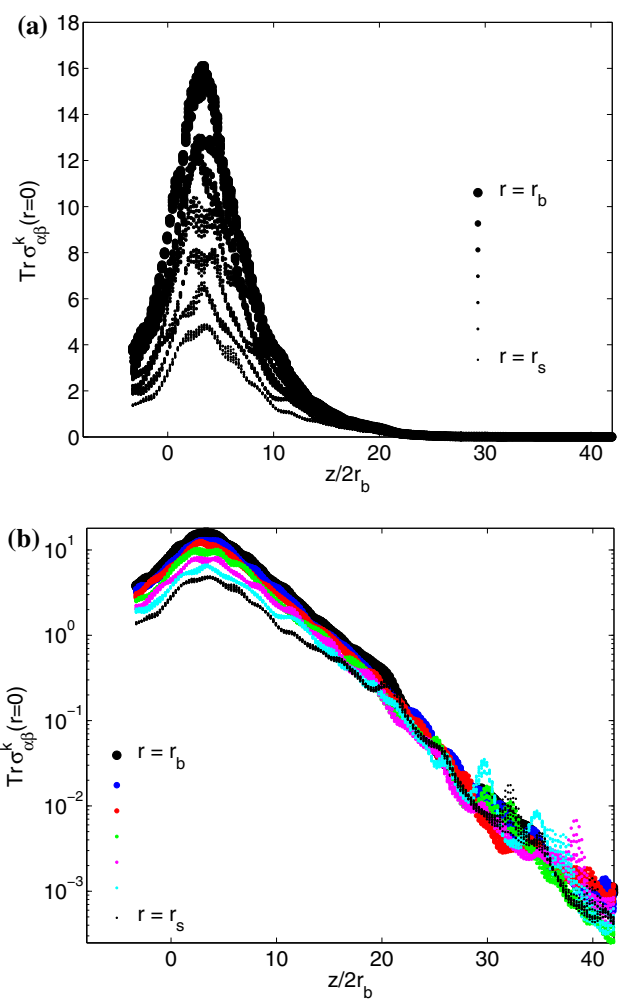
Fig. 10 Vertical profiles of the cumulative *kinetic pressure* at the center of the silo $r = 0$ and as a function of $z/2r_b$. The fields are deduced using a Gaussian coarse-graining function $\phi(\mathcal{R})$ and $w = r_b/2$

Fig. 11 In **a**, the vertical profiles of the partial *kinetic pressure* at the center of the silo $r = 0$ and as a function of $z/2r_b$ are illustrated. The fields are deduced using a Gaussian coarse-graining function $\phi(\mathcal{R})$ and $w = r_b/2$. In **b** it is shown the same in semi-log scale, the *colors* are changed to enhance the details

the particle mass, but there are no evidences supporting this hypothesis. Nevertheless, Fig. 11b illustrates that above a given height, the partial kinetic stresses of all the components equal to the same value and they decay exponentially with the distance to the orifice. As we mention before, this finite system size effect is related with the width of the silo R_c. The results presented in Fig. 11b suggest that above certain height, h_m, we obtain a well-defined mass flow. This result is practically independent of the aperture size R. Furthermore, in that region all the particles types follow the global flow, and the values of kinetic stress are practically equivalent.
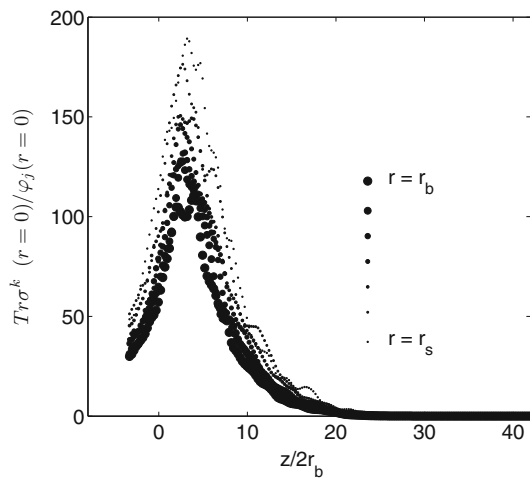
In Fig. 12, we illustrate how the partial kinetic stress compares the volume fraction of each component of the mixture φ_k. As the segregation effects are very low, the values of φ_k result proportional to the cube of the particle radio $\varphi_k \propto r_k^3$; consequently, the partial volume fraction occupied by the small particles is significantly lower than the large particles. The data of the partial *kinetic pressure* at the center of the silo $r = 0$, normalized with φ_k indicate that the small particles carry a higher fraction of kinetic stress respect to their concentration. These findings suggest that the small particles have larger velocity fluctuations than the large ones, which is consistent with previous experimental reports [32].

Summarizing, we perform large-scale DEM simulation of polydisperse granular flows in 3D silos, examining the paradoxical ideas associated with the *free-fall arch* concept. Our outcomes provide evidences that the self-similarity properties found in monodisperse spherical beads are also present when low polydispersity is taken into account. Moreover, we also found that in the range of study apertures, the size of the aperture R is the relevant scale quantifying the volumetric flow rate in silos. Additionally, we confirm that a non-trivial process occurs in a singular region above the outlet, and more

importantly, this process determines the spatial velocity profile at the silo orifice. The stress decomposition into contact and kinetic parts provides a suitable theoretical framework to distinguish between the role of force chains and velocity fluctuations. Thus, we obtain that the *contact pressure* is several orders of magnitude higher than the *kinetic pressure* and it monotonically decreases as one approaches the exit. Hence, discontinuities in the stress field are not found. This picture contrasts with the traditional view of a *free-fall arch* where assuming a stress discontinuity is the key factor when explaining the characteristic velocity at the outlet. Moreover, even though the values of kinetic stress are much smaller than the contact stress, the scaling of its spatial profile with R reveals its relevance explaining the discharge process. The general trend of the partial *kinetic pressure* profiles is very similar for all types of particles. Although we obtain

Fig. 12 The vertical profiles of the partial *kinetic pressure* at the center of the silo $r = 0$, normalized with the volume fraction of each particle type φ_i, and as a function of $z/2r_b$ are illustrated. The fields are deduced using a Gaussian coarse-graining function $\phi(\mathcal{R})$ and $w = r_b/2$

that the partial kinetic stress is larger for bigger particles, the small particles carry a higher fraction of kinetic stress respect to their concentration. Those findings suggest that the small particles have larger velocity fluctuations than the large ones, showing their lower strength of correlation with the global flow. Our results show that the coarse-graining methodology [14–17,38] is very a valuable tool, linking the microscopic details of granular media and its macroscopic behavior of polydisperse granular flows.

Compliance with ethical standards

Conflict of interest The authors declare that they have no conflict of interest.

Appendix: Discrete element modeling implementation (DEM)

The DEM implementation is a polydisperse generalization of a monodisperse hybrid CPU/GPU algorithm that allows us to efficiently evaluate the dynamics of several hundred thousand particles [37,41]. For each particle $i = 1 \ldots N$, the DEM simulation includes three translational degrees of freedom and the rotational movement is described by a quaternion formalism. We have used a linear spring approach; thus, the normal interaction force $\mathbf{F}_{ij}^n$ between the particles i with radius r_i and j with radius r_j depends linearly on the particles' overlap distance $\delta = r_i + r_j - \|\Delta R_{ij}\|$,

where $\|\Delta R_{ij}\|$ is the relative distance between the particles. Moreover, the local dissipation is introduced by a non-linear viscous damping term, which depends on the normal relative velocity $\mathbf{v}_{rel}^n$. Hence, the total normal force reads as

$$\mathbf{F}_{ij}^n = -k_n\,\delta\,\hat{n} - \gamma_n m_{eff} \mathbf{v}_{rel}^n, \qquad (9)$$

where

$$k_n = \frac{16.0}{15.0}\sqrt{R_{eff}}\,Y\left(\frac{15 m_{eff} V_c^2}{16\sqrt{R_{eff}}\,Y}\right)^{1/5} \qquad (10)$$

and

$$\gamma_n = \sqrt{\frac{4 m_{eff} k_n}{1 + \left(\frac{\pi}{\ln(e_n)}\right)^2}} \qquad (11)$$

represent the damping coefficient, $m_{eff} = m_i m_j/(m_i + m_j)$, $R_{eff} = r_i r_j/(r_i + r_j)$, and Y is the particles Young's modulus. The tangential component F_{ij}^t also includes an elastic term and a viscous term,

$$\mathbf{F}_{ij}^t = -k_t\boldsymbol{\xi} - \gamma_t m_{eff} \mathbf{v}_{rel}^t, \qquad (12)$$

where γ_t is a damping coefficient and $\mathbf{v}_{rel}^t$ is the tangential relative velocity of the overlapping pair. The variable $|\boldsymbol{\xi}|$ represents the elongation of an imaginary spring with elastic constant k_t. As long as there is an overlap between the interacting particles, $\boldsymbol{\xi}$ increases as $d\boldsymbol{\xi}/dt = \mathbf{v}_{rel}^t$ [13]. The elastic tangential elongation $\boldsymbol{\xi}$ is kept orthogonal to the normal vector [15] and it is truncated as necessary to satisfy the Coulomb constraint $|\mathbf{F}_{ij}^t| < \mu|\mathbf{F}_{ij}^n|$, where μ is the friction coefficient. The equations of motion are integrated using Fincham's leap-frog algorithm (rotational) [42] and a Verlet Velocity algorithm (translational) [43].

In all the simulations reported here, the used contact parameters correspond to particles with a Young's modulus $Y = 120\,GPa$, normal restitution coefficient $e_n = 0.88$, density $\rho_p = 7520$ kg/m^3, and friction $\mu = 0.5$. We set $\frac{k_t}{k_n} = \frac{2}{7}$ and $\frac{\gamma_t}{\gamma_n} = 0.1$, and gravitational acceleration $g = 10\,m/s^2$. In all cases, the molecular dynamics time step was set as $\Delta t = \frac{t_c}{50} = 6.3 \times 10^{-7}\,s$, where t_c is approximately equal to time of contact between two small particles $t_c = \pi\sqrt{\frac{m_{eff}}{2k_n}}$.

References

1. Rubio-Largo SM, Janda A, Maza D, Zuriguel I, Hidalgo RC (2015) Disentangling the free-fall arch paradox in silo discharge. Phys Rev Lett 114:238002

2. Sperl M (2006) Experiments on corn pressure in silo cells: translation and comment of janssen's paper from 1895. Granul Matter 8(2):59–65

3. Brown RL, Richards JC (1970) Principles of powder mechanics: essays on the packing and flow of powders and bulk solids. Pergamon Press, Oxford

4. Nedderman RM (1992) Statistics and kinematics of granular materials. Cambridge University Press, Cambridge

5. Mathews JC, Wei Wu (2016) Model tests of silo discharge in a geotechnical centrifuge. Powder Technol 293:3–14

6. Beverloo WA, Leniger HA, van de Velde J (1961) The flow of granular solids through orifices. Chem Eng Sci 15(34):260–269

7. Mankoc C, Janda A, Arévalo R, Pastor JM, Zuriguel I, Garcimartín A, Maza D (2007) The flow rate of granular materials through an orifice. Granul Matter 9(6):407–414

8. Janda A, Zuriguel I, Maza D (2012) Flow rate of particles through apertures obtained from self-similar density and velocity profiles. Phys Rev Lett 108:248001

9. Kamrin K, Koval G (2012) Nonlocal constitutive relation for steady granular flow. Phys Rev Lett 108:178301

10. Henann DL, Kamrin K (2014) Continuum modeling of secondary rheology in dense granular materials. Phys Rev Lett 113:178001

11. Vivanco F, Rica S, Melo F (2012) Dynamical arching in a two dimensional granular flow. Granul Matter 14(5):563–576

12. Van Zuilichem DJ, Van Egmond ND, De Swart JG (1974) Density behaviour of flowing granular material. Powder Technol 10:161–169

13. Pöschel T, Schwager T (2005) Computational granular dynamics. Springer, Berlin

14. Goldhirsch I (2010) Stress, stress asymmetry and couple stress: from discrete particles to continuous fields. Granul Matter 12:239–252

15. Weinhart T, Thornton AR, Luding S, Bokhove O (2012) Closure relations for shallow granular flows from particle simulations. Granul Matter 14(4):531–552

16. Weinhart T, Hartkamp R, Thornton AR, Luding S (2013) Coarse-grained local and objective continuum description of three-dimensional granular flows down an inclined surface. Phys Fluids 25(7):070605

17. Weinhart T, Labra C, Luding S, Ooi JY (2016) Influence of coarse-graining parameters on the analysis of DEM simulations of silo flow. Powder Technol 293:138–148. doi:10.1016/j.powtec.2015.11.052

18. Valdes JR, Santamarina JC (2007) Particle transport in a nonuniform flow field: retardation and clogging. Appl Phys Lett 90(24):244101

19. Katsuragi H, Abate AR, Durian DJ (2010) Jamming and growth of dynamical heterogeneities versus depth for granular heap flow. Soft Matter 6:3023–3029

20. Zuriguel I, Janda A, Garcimartín A, Lozano C, Arévalo R, Maza D (2011) Silo clogging reduction by the presence of an obstacle. Phys Rev Lett 107:278001

21. Kanzaki T, Acevedo M, Zuriguel I, Pagonabarraga I, Maza D, Hidalgo RC (2011) Stress distribution of faceted particles in a silo after its partial discharge. Eur Phys J E 34:133

22. Lozano C, Lumay G, Zuriguel I, Hidalgo RC, Garcimartín A (2012) Breaking arches with vibrations: the role of defects. Phys Rev Lett 109:068001

23. Thomas CC, Durian DJ (2013) Geometry dependence of the clogging transition in tilted hoppers. Phys Rev E 87:052201

24. Hidalgo RC, Lozano C, Zuriguel I, Garcimartín A (2013) Force analysis of clogging arches in a silo. Granul Matter 15(6):841–848

25. Aguirre MA, Grande JG, Calvo A, Pugnaloni LA, Géminard J-C (2010) Pressure independence of granular flow through an aperture. Phys Rev Lett 104:238002

26. Zuriguel I, Parisi DR, Hidalgo RC, Lozano C, Janda A, Gago PA, Peralta JP, Ferrer LM, Pugnaloni LA, Clément E, Maza IPD, Garcimartín A (2014) Clogging transition of many-particle systems flowing through bottlenecks. Sci Rep 4:7324

27. Kamath S, Kunte A, Doshi P, Orpe AV (2014) Flow of granular matter in a silo with multiple exit orifices: jamming to mixing. Phys Rev E 90:062206

28. Benyamine M, Djermane M, Dalloz-Dubrujeaud B, Aussillous P (2014) Discharge flow of a bidisperse granular media from a silo. Phys Rev E 90:032201

29. Thomas CC, Durian DJ (2015) Fraction of clogging configurations sampled by granular hopper flow. Phys Rev Lett 114:178001

30. Gutiérrez G, Colonnello C, Boltenhagen P, Darias JR, Peralta-Fabi R, Brau F, Clément E (2015) Silo collapse under granular discharge. Phys Rev Lett 114:018001

31. Gray JMNT, Thornton AR (2005) A theory for particle size segregation in shallow granular free-surface flows. Proc R Soc Lond A 461(2057):1447–1473

32. Hill KM, Zhang J (2008) Kinematics of densely flowing granular mixtures. Phys Rev E 77:061303

33. Fan Y, Hill KM (2011) Theory for shear-induced segregation of dense granular mixtures. New J Phys 13(9):095009

34. Prescott JK, Carson JW (2000) Analyzing and overcoming industrial blending and segregation problems. Springer, Dordrecht, pp 89–101

35. Samadani A, Pradhan A, Kudrolli A (1999) Size segregation of granular matter in silo discharges. Phys Rev E 60:7203–7209

36. Rubio-Largo SM, Lind PG, Maza D, Hidalgo RC (2015) Granular gas of ellipsoids: analytical collision detection implemented on gpus. Comput Part Mech 2(2):127–138

37. Hidalgo RC, Kanzaki T, Alonso-Marroquin F, Luding S (2013) On the use of graphics processing units (gpus) for molecular dynamics simulation of spherical particles. AIP Conf Proc 1542:169–172

38. Tunuguntla DR, Thornton AR, Weinhart T (2016) From discrete elements to continuum fields: extension to bidisperse systems. Comput Part Mech 3(3):349–365

39. Madrid M, Asencio K, Maza D (2016) Soft matter. Submitted

40. Artoni R, Richard P (2015) Average balance equations, scale dependence, and energy cascade for granular materials. Phys Rev E 91:032202

41. Owens JD, Houston M, Luebke D, Green S, Stone JE, Phillips JC (2008) Gpu computing. Proc IEEE 96(5):879–899

42. Fincham D (1992) Leapfrog rotational algorithms. Mol Simul 8(3–5):165–178

43. Verlet L (1968) Computer "experiments" on classical fluids. ii. equilibrium correlation functions. Phys Rev 165(1):201–214